INFERENCE OF HEATING PROPERTIES FROM "HOT" NON-FLARING PLASMAS IN ACTIVE REGION CORES II. NANOFLARE TRAINS

W. T. Barnes
Department of Physics & Astronomy, Rice University, Houston, TX 77251-1892

P. J. Cargill
Space and Atmospheric Physics, The Blackett Laboratory, Imperial College, London SW7 2BW and
School of Mathematics and Statistics, University of St. Andrews, St. Andrews, Scotland KY16 9SS

and

S. J. Bradshaw
Department of Physics & Astronomy, Rice University, Houston, TX 77251-1892
Draft version April 4, 2016

ABSTRACT

Faint, high-temperature emission in active region cores has long been predicted as a signature of nanoflare heating. However, the detection of such emission has proved difficult due to a combination of the efficiency of thermal conduction, non-equilibrium ionization, and inadequate instrument sensitivity. This second paper in our series on hot non-flaring plasma in active regions aims to show how the assumption of electron-ion equilibrium leads to misleading conclusions regarding the hot emission. We have used an efficient two-fluid hydrodynamic model to carry out a parameter exploration in preferentially heated species, heating event frequency, and the power-law index determining the distribution of event energies. By computing the emission measure distributions and calculating their "hotward" slopes, we have concluded that not treating the electron and ion populations separately leads to a mischaracterization of the hot emission. Additionally, we find that, while emission due to separate electron and ion heating differs greatly hotward of the peak, the respective coolward emission measure slopes are similar such that a distinction between the heating of one species over another based on this criteria alone is not possible.

1. INTRODUCTION

Heating of the solar corona by nanoflares, first proposed by Parker (1988), has become one of the most favored and contentious coronal heating models (Cargill 1994; Cargill & Klimchuk 2004; Klimchuk 2006). The term *nanoflare* has now become synonomous with impulsive heating in the energy range $10^{24} - 10^{27}$ erg, with no specific assumption regarding the underlying physical mechanism; though its origin is almost certainly magnetic.

Cargill (1994) and Cargill & Klimchuk (2004) have predicted that emission measure distributions resulting from nanoflare models should be wide and have a faint, high-temperature (8-10 MK) component and thus a steep hotward slope, the so-called "smoking gun" of nanoflare heating. Unfortunately, observing this high-temperature emission is difficult and in some cases impossible. The reason for this difficulty is twofold. First, thermal conduction is a very efficient cooling mechanism at high temperatures and large spatial temperature gradients. When a loop is heated impulsively, its temperature rises quickly while the increase in density lags behind. By the time the density has increased sufficiently (due to chromospheric evaporation brought about by the response of the transition region to the strong downward coronal heat flux) to allow for an appreciable amount of emission (recalling EM $\propto n^2$), thermal conduction has cooled the loop far below its initial hot temperature, making a direct detection of ~ 10 MK plasma very difficult.

The second reason for this difficulty is non-equilibrium ionization (NEI). It is usually assumed that the observed emission lines, because of their known formation temperatures, are a direct indicator of the plasma temperature. However, if the heating (or cooling) timescale is shorter than the ionization equilibration timescale, the time it takes for the ion population to settle into the assumed charge state, an equilibrium assumption can lead to a misdiagnosis of the plasma temperature. This makes signatures of hot, nanoflare-heated plasma especially difficult to detect if the high temperatures persist for less than the ionization timescale (Bradshaw & Cargill 2006; Bradshaw & Klimchuk 2011; Reale & Orlando 2008).

Several workers have modeled both steady and impulsive heating in coronal loops.

Despite these difficulties, various attempts have been made to observe this faint high-temperature emission. Using the broadband X-Ray Telescope (XRT) (Golub et al. 2007) on board the *Hinode* spacecraft (Kosugi et al. 2007), Schmelz et al. (2009) and Reale et al. (2009) show a faint hot component in the reconstructed DEM curves. However, since the channels on such broadband instruments can often be polluted by low-temperature emission, the reliability of such measurements depends on the filtering technique used. Additionally, Winebarger et al. (2012) showed that combinations of measurements from XRT and the Extreme-ultraviolet Imaging Spectrometer (EIS) (Culhane et al. 2007), also on *Hinode*, leave a "blind spot" in the EM $-$ T space conincident with the

will.t.barnes@rice.edu

range where evidence for nanoflare heating is likely to be found.

Unambiguous observational evidence of nanoflare heating must come from pure spectroscopic measurements (see Brosius et al. 2014). Additionally, new instruments with higher spatial and temporal resolution, such as *IRIS* (De Pontieu et al. 2014) and the *Hi-C* sounding rocket (Cirtain et al. 2013) have provided encouraging results for impulsive heating (Testa et al. 2013, 2014). Future missions like the Marshall Grazing Incidence X-ray Spectrometer (MaGIXS) (Kobayashi et al. 2011; Winebarger 2014), with a wavelength range of 6-24 Å and a temperature range of $6.2 < \log T < 7.2$, aim to probe this previously poorly-resolved portion of the coronal spectrum in hopes of better quantifying the presence of faint, high-temperature plasma.

An important parameter for any proposed coronal heating mechanism is the frequency of energy release. Nanoflare heating is often classified as either *high-frequency* or *low-frequency* heating. In the case of high-frequency heating, t_N, the time between successive events, is such that $t_N \ll \tau_c$, where τ_c is the loop cooling time, and in the case of low-frequency heating $t_N \gg \tau_c$. Steady heating is just high-frequency heating in the limit $t_N \to 0$.

One strategy for constraining the nanoflare model is analysis of modeled and observed emission measure distributions for signatures of impulsive heating in active region (AR) cores. As with cool emission, hot emission is also often described by a power-law relation of the form EM $\propto T^{-b}$. Typically, this power-law fit to the emission measure is done "hotward" of the peak, usually in the range $6.6 \lesssim \log T \lesssim 7.2$. However, measured values of these hotward slopes are poorly constrained due to both the magnitude of emission and the lack of available spectroscopic data in this temperature range. Warren et al. (2012), using spectral measurements from EIS, provided hotward fits for EM reconstructions for a large number of ARs. All measured slopes fell in the range $6.1 < b < 10.3$, with large uncertainties on each hotward fit.

In our first paper, Barnes et al. (2016) (Paper I, hereafter), we studied the effect of pulse duration, flux limiting, and NEI on hot emission from single nanoflares. In this second paper in our series on hot emission in AR cores, we use an efficient two-fluid hydrodynamic model to explore the effect of repeated impulsive heating events of varying frequency. In particular, we look at how the hot emission is affected by heating preferentially the electrons or the ions with events drawn from a power-law distribution. Additionally, we consider the effect of scaling the inter-event waiting time to the event energy and how NEI may affect hot emission measure slopes.

Section 2 discusses the numerical model we have used to conduct this study and the parameter space we have investigated. Section 3 shows the resulting emission measure curves and slopes for the electron and ion heating cases as well as the equivalent single-fluid cases. In Section 4, we discuss the implications of two-fluid effects in the context of hot and cool emission measure slopes and the nanoflare heating model. Finally, Section 5 provides some concluding comments on our findings.

2. METHODOLOGY

2.1. *Numerical Model*

1D hydrodynamic models are excellent tools for computing field-aligned quantities in coronal loops. However, because of the small cell sizes needed to resolve the transition region and consequently small timesteps demanded by thermal conduction, the use of such models in large parameter space explorations is made impractical by long computational runtimes (Bradshaw & Cargill 2013). We use the popular 0D enthalpy-based thermal evolution of loops (EBTEL) model (Klimchuk et al. 2008; Cargill et al. 2012a,b, 2015). This model, which has been successfully benchmarked against the 1D hydrodynamic HYDRAD code of Bradshaw & Cargill (2013), computes, with very low computational overhead, time-dependent, spatially-averaged loop quantities.

In order to treat the evolution of the electron and ion populations separately, we use a modified version of the usual EBTEL equations. This amounts to computing spatial averages of the two-fluid hydrodynamic equations over both the transition region and corona. A full description and derivation of these equations can be found in the appendix of Paper I. The relevant two-fluid pressure and density equations are,

$$\frac{d}{dt}\bar{p}_e = \frac{\gamma - 1}{L}\left[\psi_{TR} - (\mathcal{R}_{TR} + \mathcal{R}_C)\right] + \tag{1}$$

$$k_B \bar{n} \nu_{ei}(\bar{T}_i - \bar{T}_e) + (\gamma - 1)\bar{Q}_e, \tag{2}$$

$$\frac{d}{dt}\bar{p}_i = -\frac{\gamma - 1}{L}\psi_{TR} + k_B \bar{n} \nu_{ei}(\bar{T}_e - \bar{T}_i) + \tag{3}$$

$$(\gamma - 1)\bar{Q}_i, \tag{4}$$

$$\frac{d}{dt}\bar{n} = \frac{c_2(\gamma - 1)}{c_3 \gamma L k_B \bar{T}_e}\left(\psi_{TR} - F_{ce,0} - \mathcal{R}_{TR}\right), \tag{5}$$

where ν_{ei} is the electron-ion binary Coulomb collision frequency and ψ_{TR} is a term included to maintain charge and current and neutrality. These equations are closed by the equations of state $p_e = k_B n T_e$ and $p_i = k_B n T_i$. A full discussion and derivation of these 0D two-fluid equations can be found in the appendix of Paper I.

Include some temperature and density profiles for nanoflare trains in here somehow? May need to move to next section...

2.2. *Energy Budget*

Details about static parameters for all runs. All events are modeled as triangular pulses of fixed duration $\tau = 200$ s.

We define our heating function in terms of a series of discrete heating events plus a static background heating to ensure that the loop does not drop to unphysically low temperatures and densities between events. Thus, for loop half-length L and cross-sectional area A, for a triangular heating pulse of duration τ, the total event energy is $\varepsilon = LAH\tau/2$, where H is the heating rate. Each run will consist of N heating events, each with peak amplitude H_i, and a steady background value of $H_{bg} = 3.5 \times 10^{-5}$ erg cm^{-3} s^{-1}.

Recent observations have suggested that loops in AR cores are maintained at an equilibrium temperature of $T_{peak} \approx 4$ MK (Warren et al. 2011, 2012). Using our modified two-fluid EBTEL model, we have estimated the corresponding time-averaged volumetric heating rate for
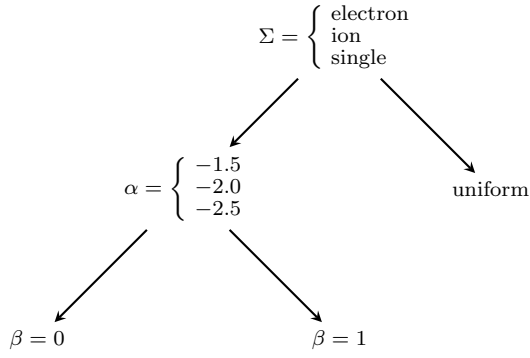
FIG. 1.— Total Parameter space covered. Σ indicates the species that is heated, where "single" indicates a single-fluid model. α is the power-law index and β indicates the scaling in the relationship $Q \propto T_N^\beta$, where $\beta = 0$ corresponds to the case where t_N and the event energy are independent. Note that (3 α values) × (2 β values) + uniform heating = 7 different types of heating functions. <mark>Adjust depending on what value of β we use in the end.</mark>

a loop of half-length $L = 40$ Mm to be $H_{eq} \sim 4.5 \times 10^{-3}$. In the single-fluid EBTEL model, this value is slightly lower because losses due to electron-ion collisions are ignored. Thus, to maintain an emission measure peaked about T_{peak}, for triangular pulses, the individual event heating rates are constrained by

$$H_{eq} = \frac{1}{t_{total}} \sum_{i=1}^{N} \int_{t_i}^{t_i+\tau} dt\ h_i(t) = \frac{\tau}{2t_{total}} \sum_{i=1}^{N} H_i, \quad (6)$$

where t_{total} is the total simulation time. Note that if $H_i = H_0$ for all i, the uniform heating rate H_0 is $H_0 = 2t_{total}H_{eq}/N\tau$. Thus, for $L = 40$ Mm, $A = 10^{14}$ cm^2, the total amount of energy injected into the loop by one heating event for a loop heated by $N = 20$ nanoflares in $t_{tot} = 8 \times 10^4$ s is $\varepsilon = LAt_{total}H_{eq}/N \approx 7.2 \times 10^{24}$ erg, consistent with the energy budget of the Parker nanoflare model.

Determining the heating frequency in AR cores will help to place constraints on the source(s) of heat in the corona. We define the heating frequency in terms of the waiting time, t_N, between successive heating events. Following Cargill (2014), the range of waiting times is $250 \leq t_N \leq 5000$ s in increments of 250 s, for a total of 20 different possible heating frequencies. Additionally, t_N can be written as $t_N = (t_{total} - N\tau)/N$, where we fix $T = 8 \times 10^4$ s. Note that because t_{total} and τ are fixed, as t_N increases, N decreases. Correspondingly, ε_i, the energy injected per event, increases according to Equation 6 such that the total energy injected per run is constant, regardless of t_N.

According to the nanoflare heating model of Parker (1988), turbulent loop footpoint motions twist and stress the field, leading to a buildup and subsequent release of energy. Following Cargill (2014), we let $\varepsilon_i \propto t_{N,i}^\beta$, where $\varepsilon_i, t_{N,i}$ are the total energy and waiting time following event i, respectively, and $\beta = 1, 2$ such that the event energy scales either linearly or quadratically with the waiting time. The reasoning for such an expression is as follows. Bursty, nanoflare heating is thought to arise from the stressing and subsequent relaxation of the coronal field. If a sufficient amount of energy is released into
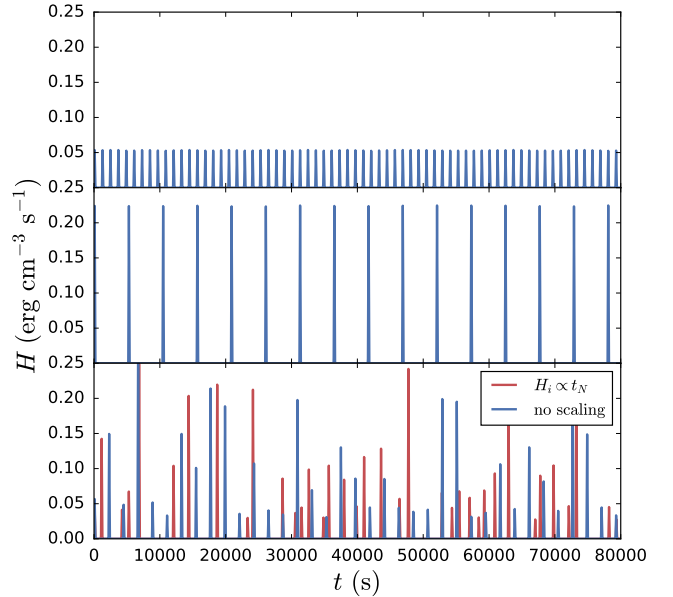

FIG. 2.— **Top**: uniform heating amplitudes for $t_N = 1000$ s; **Middle**: uniform heating amplitudes for $t_N = 5000$ s; **Bottom**: Heating amplitudes drawn from a power-law distribution with index $\alpha = -1.5$. The events shown in red have wait times that depend on the previous event energy while the events shown in blue have uniform wait times. The mean wait time in both cases is $\langle t_N \rangle = 2000$ s.

the loop, the field will need enough time to "unravel" and "wind up" again before the next event such that the subsequent waiting time is large. Conversely, if only a small amount of energy is released, the field will require a shorter unwinding time, resulting in a shorter interval between the subsequent events. Thus, this scaling provides a way to incorporate a more physically motivated heating function into a hydrodynamic model which cannot self-consistently determine the heat input based on the evolving magnetic field. Figure 2 shows the various heating functions used for several example t_N values.

2.3. Heating Statistics

We compute the peak heating rate per event in two different ways: 1) the heating rate is uniform such that $H_i = H_0$ for all i and 2) H_i is chosen from a power-law distribution with index α where $\alpha = -1.5, -2.0$, or -2.5. For the second case, it should be noted that, when $t_N \approx 5000$ s, $N \sim 20$ events, meaning a single run does not accurately represent the distribution of index α. Thus, a sufficiently large number of runs, N_R, are computed for each t_N to ensure that the total number of events is $N_{tot} = N \times N_R \sim 10^4$ such that the distribution is well-represented. Figure 1 shows the parameter space we will explore. For each set of parameters and waiting time t_N, we compute the resulting emission measure distribution for N events in a period t_{total}. This procedure is repeated N_R times until $N \times N_R \sim 10^4$ is satisfied.

2.4. Non-equilibrium Ionization

When considering the role of nanoflares in the production of hot plasma in AR cores, it is important to take non-equilibrium ionization (NEI) into account (Bradshaw & Cargill 2006; Reale & Orlando 2008). In a steady heating scenario, the ionization state is an adequate mea-

sure of the electron plasma temperature. Because the heating timescale is long (effectively infinite), the ionization state has plenty of time to come into equilibrium with the electron temperature.

In a nanoflare train, when the heating frequency is high, the loop is not allowed to drain or cool sufficiently between events, meaning the ionization state is kept at or near equilibrium. However, as the heating frequency decreases, the loop is allowed to cool and drain more and more during the inter-event period. If the heating occurs on a short enough timescale, the ionization state will not be able to reach equilibrium with the electron plasma before the loop undergoes rapid cooling by thermal conduction. Furthermore, if the frequency is sufficiently low so as to allow the loop to drain during the inter-event period, the ionization equilibrium timescale will increase. Thus, in the context of intermediate- to low-frequency nanoflares, NEI should be considered.

As in Paper I, we use the numerical code[1] outlined in Bradshaw (2009) to compute the non-equilibrium ionization states and the corresponding effective electron temperature, T_{eff} that would be inferred by assuming ionization equilibrium. Using T_{eff}, we are then able to compute a corresponding NEI emission measure distribution.

3. RESULTS

In our 0D model, the emission measure is calculated using the familiar expression $EM = n^2(2L)$, where L is the loop half-length. We consider a temperature range of $4.0 \leq \log T \leq 8.5$ with bin sizes of $\Delta \log T = 0.01$. At each iteration i, the coronal temperature range $[T_0, T_a]$ is calculated from $\bar{T}_e$. For each bin that falls within $[T_0, T_a]$, $\bar{n}_i^2(2L)$ is added to that bin, where $\bar{n}_i$ is the spatially-averaged number density at iteration i. The emission measure in each bin is then averaged over the entire simulation period. When measured observationally, $EM(T)$ is a line-of-sight quantity. Assuming an aspect ratio (i.e. ratio of loop length to loop width) of 10, we apply a correction factor $1/10$ to all calculated EM curves. We do not attempt to apply an advanced forward modeling treatment here and instead reserve such an approach for a future paper. However, while effects due to NEI are neglected in our parameter space exploration, in Subsection 3.3 we consider the emission measure due to T_{eff}, the effective temperature due to NEI, for several test cases in order to diagnose how this might affect our calculated emission measure slopes.

For each species, type of power-law heating function, and waiting time t_N, N_R emission measure curves are calculated. Because drawing event amplitudes from a power-law distribution introduces random fluctuations into our model, we must be sure to account for the full range of effects due to the distribution. This is especially true in the low-frequency regime, when $T_N \geq \tau_{cool}$, the cooling timescale, and there are fewer events per run. In this case, one or two especially strong heating events can lead to an extremely enhanced hotward emission measure; conversely, a run with only small events will lead to a diminished hotward slope. Thus, the mean EM curve

of each set of N_R runs can be said to reasonably represent the expected hot emission for a given t_N.

To characterize the emission measure, we compute the slopes on both the cool and hot sides of the peak. To be consistent with past observational and computational studies of cool emission (see Bradshaw et al. 2012, and references therein), we fit the cool slope on the interval $6.0 \leq \log T \leq 6.6$. Contrastingly, past studies of hot emission are less abundant; thus, the "hot" region where the EM is thought to follow a power-law is far less constrained. In order to best describe the steepness of the emission measure hotward of the peak, we choose to fit EM between the temperatures at which the emission measure is 99% and 92% of the peak value. We have no physical reason for choosing these particular bounds, but note that on this interval, the mean hotward emission is reasonably well-described by a power-law relationship. Fitting too close to the wide peak leads to misleadingly shallow slopes while fitting too close to the steep drop near $\log T \sim 7.5$ results in steep slopes not particularly representative of the hotward emission. We perform the fit using the Levenberg-Marquardt algorithm for least-squares curve fitting as implemented in the SciPy scientific Python package (van der Walt et al. 2011).

3.1. Emission Measure Distributions

Figure 3 and Figure 4 show the results of our emission measure study for the two distinct cases where only the electrons are heated and only the ions are heated with $\alpha = -2.5, \beta = 1$ for a loop half-length of 40 Mm, consistent with Paper I. The panels on the left show the mean EM for all t_N, where the average is taken over all N_R runs. There is an artifical spacing of $\Delta \log EM = 0.2$ between each curve so that they can be easily distinguished from each other. The blue (red) lines indicate the cool (hot) power-law fits, where the slopes of the lines are the averages taken over all N_R runs. We note that the EM, for all t_N, peaks at approximately 4 MK ($10^{6.6}$ K), consistent with the constraints laid out in Subsection 2.2. The top right panels show these average slope values as a function of t_N. The error bars indicate one standard deviation as calculated from the distribution of all N_R runs.

Lastly, the bottom right panels show the first derivative as a function of temperature, $d \log EM/d \log T$, computed using central differences. The color scheme and line styles correspond to the emission mesure curves in the left panel. As in Paper I, we compute the derivative in an effort to better assess at what temperatures the emission measure is not well described by a power-law.

We first briefly consider the calculated cool emission measure slopes. Looking at the top right panels of Figure 3 and Figure 4, we note that in the cases of electron and ion heating, the cool emission measure slopes are consistent with both observational and modeling studies of cool emission in AR cores, having values that fall within the range $2 \leq a \leq 5$ (Bradshaw et al. 2012, and references therein). Furthermore, the cool slopes computed using our new modified EBTEL model, with a heating function of the form $Q \propto T_N^{\beta}$, are consistent with those values reported in Cargill (2014) and show a dependence on the waiting time t_N.

Additionally, looking at the bottom right panels of

---

[1] This code has been made freely available by the author and can be downloaded at: https://github.com/rice-solar-physics/IonPopSolver
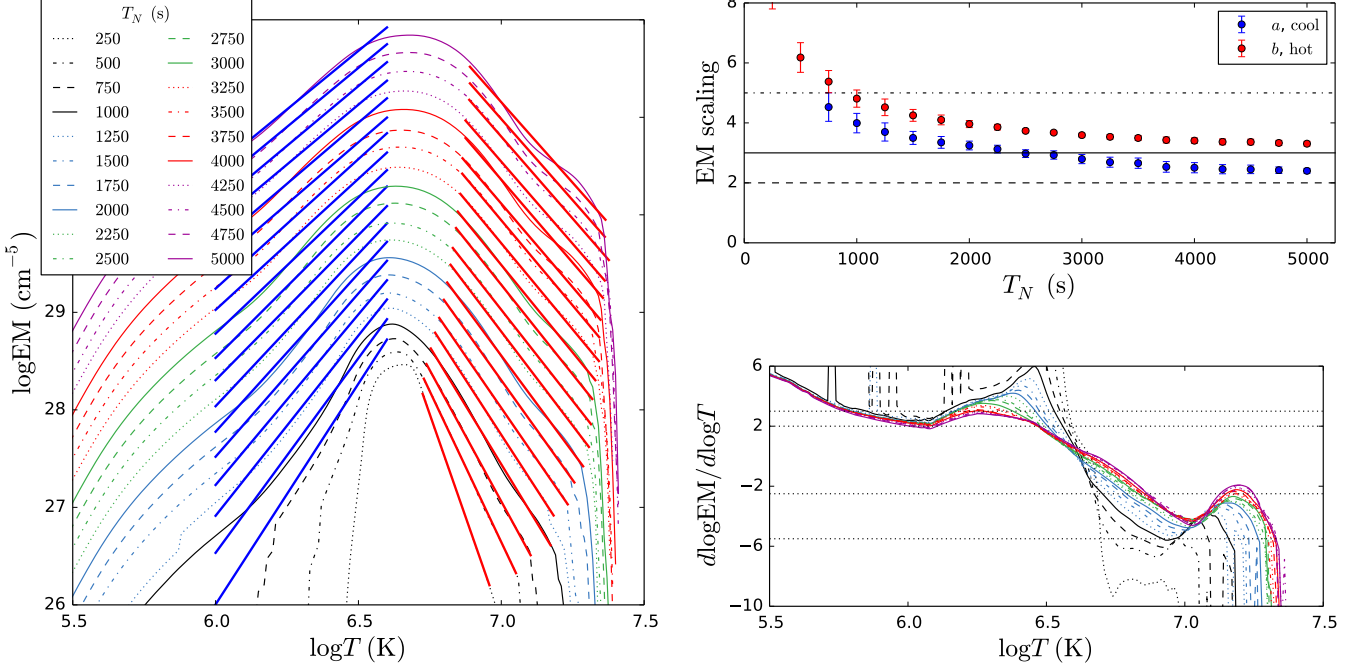
FIG. 3.— $\alpha = -2.5$, $\beta = 1$, $L = 40$ Mm, electron heating. **Left:** $\log \mathrm{EM}$ as a function of $\log T$ for all values of t_N. There is an artificial spacing of $\Delta \log \mathrm{EM} = 0.2$ between each curve. The bold blue (red) lines on either side of the peak show the linear fit to the cool (hot) emission. **Top right:** Average slopes from power-law fits to all N_R curves as a function of t_N. The error bars indicate one standard deviation from the distribution of N_R fits. In the case of hot slopes, the absolute value is shown. The dashed, solid, and dot-dashed reference lines are placed at 2, 3, and 5 respectively. **Bottom right:** Derivative of $\log \mathrm{EM}$ with respect to $\log T$. The dotted reference lines are placed at -5.5, -2.5, 2, and 3. The legend is the same as the left panel.

Figure 3 and Figure 4, we see that, within the range $6.0 \leq \log T \leq 6.6$, the EM is reasonably well-described by a power-law, where $2 \lesssim d \log \mathrm{EM}/d \log T \lesssim 3$. Comparing the cases of electron and ion heating for both the cool slopes and $d \log \mathrm{EM}/d \log T$ on $6.0 \leq \log T \leq 6.6$, there are no substantial differences for all values of t_N considered.

This is not the case for the hot emission measure. Looking first at the case of electron heating in Figure 3, we note that there is a pronounced "hot shoulder" in the emission measure (left panel) just above 10^7 K for $T_N \gtrsim 2000$ s. This feature is even more evident when looking at the derivative of EM in the bottom right panel of Figure 3. The peak between 10^7 and $10^{7.5}$ K shows how the EM flattens out around 10^7 K, indicating an enhanced hot emission measure. Considering the large range of values of $d \log \mathrm{EM}/d \log T$ on the interval over which the fit was performed, we acknowledge that a single power-law fit is not a good description of the hot emission measure in the case of electron heating.

Contrastingly, we have not calculated the hot emission measure slopes for the case of ion heating. Looking at the left panel of Figure 4, for $T_N \gtrsim 1000$ s, the EM peak is wide with a sharp cutoff just above 10^7 K. There is no substantial emission measure component above 10^7 K and, consequently, no hot shoulder as in the electron heating case. Applying the fitting procedure outlined above to the hot emission in the case of ion heating yields meaningful results for only a few short t_N. Thus, as in the case of electron heating, the resulting hot emission measure from ion heating is also not well described by a power-law. The lower right panel of Fig-

ure 4 further highlights this by showing that around 10^7 K, $d \log \mathrm{EM}/d \log T \rightarrow -\infty$.

3.2. *Pre-nanoflare Density*

Figure 5 shows the same results as Figure 3 and Figure 4, but for the single-fluid case in which electron-ion equilibrium is assumed at all times. To compute these EM curves, we have used the original, single-fluid EBTEL model as described in Klimchuk et al. (2008) and Cargill et al. (2012a). The equivalent parameter space that was investigated with the modified two-fluid EBTEL model is explored with the single-fluid EBTEL code as well.

We compute the hot and cool emission measure slopes in the same manner as the electron and ion heating cases. We first note that the cool emission measure slopes are comparable to those in both the electron and ion heating cases. In particular, we find $2 \lesssim a \lesssim 5$ for all values of t_N as expected. Again, we confirm the validity of our linear fit to the cool emission by computing the derivative $d \log \mathrm{EM}/d \log T$ in the lower right panel of Figure 5. For $T_N \gtrsim 2000$ s, the slope is bounded between 2 and 3 on the interval $6.0 \leq \log T \leq 6.6$.

The hot emission measure in the single-fluid case differs significantly from the two-fluid case. In contrast to the electron heating case in Figure 3, the EM curves in the left panel of Figure 5 show no hot shoulder. This is further confirmed by the lower right panel; the derivative, in contrast to the electron heating case, shows no peak near 10^7 K. For low t_N, $d \log \mathrm{EM}/d \log T$ is monotonically decreasing for $\log T \gtrsim 6.6$. For $T_N \geq 3000$ s, $d \log \mathrm{EM}/d \log T$ is relatively flat for $\log T \geq 7.0$, indicat-
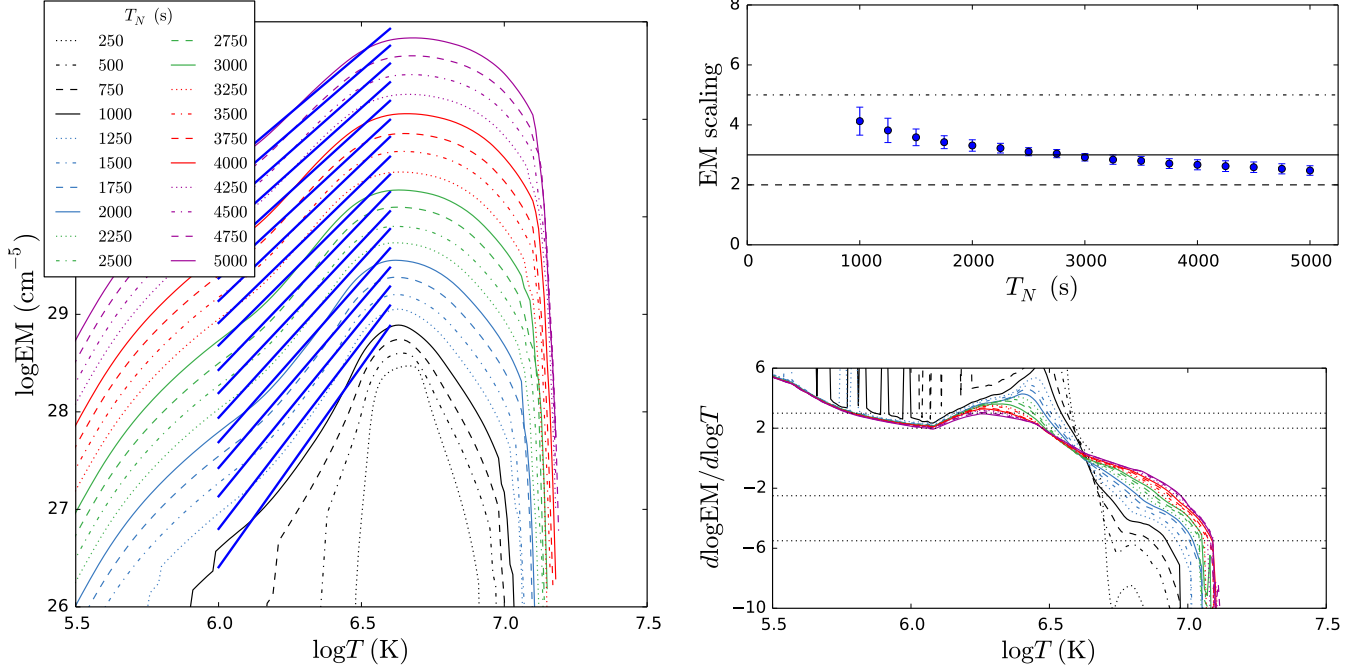
FIG. 4.— Same as Figure 3, but for the case in which all of the heating is given to the ions.

ing that a power-law provides a good description of the hot emission in this region. This is confirmed by noting the agreement between the fit lines and the EM curves in the left panel.

Comparing the top right panels of Figure 5 and Figure 3 further highlights the enhanced hot emission in the electron case. For high t_N, the hot emission slopes in the electron case converge to a value just above 3; for the single-fluid case, the hot slopes converge to approximately 4.5. Thus, while a single power-law is not a good descriptor for the hot emission in the case of electron heating, the slope still captures the enhanced hot shoulder relative to the weaker hot emission of the single-fluid case. Additionally, comparing the single-fluid case to the ion heating case in Figure 4, it is obvious that the single-fluid case shows a great deal more hot emission as the EM curves in the left panel of Figure 5 extend well above 10^7 K while those in the left panel of Figure 4 show a steep cutoff at temperatures just above the peak.

3.3. *Hot Plasma Diagnostics*

As mentioned in Section 1, NEI can make it difficult to observe emission signatures from nanoflare-heated plasma because the heating timescale is shorter than the ionization timescale such that the charge state of the plasma is not representative of the plasma temperature. In order to diagnose how NEI might affect hot emission measure slopes, we use n and T_e profiles from our modified EBTEL code along with the method outlined by Bradshaw (2009) to compute T_{eff}, the temperature that would be measured based on the actual ionization states. An effective emission measure distribution, EM_{eff}, can then be calculated. Following Paper I, we use iron (Fe) and the ionization states Fe IX through FeXXV.

As the calculation of T_{eff} is significantly more expensive than an EBTEL calculation, we do not compute

EM_{eff} for the entire parameter space and instead consider only a small number of single-pulse test cases of duration $\tau_H = 100$ s and peak heating rate $H_0 = 0.8$ erg cm^{-3} s^{-1}. Figure 6 shows temperature and density profiles (left column) and emission measure distributions (right column) for the cases where NEI is (dashed) and is not (solid) included. These profiles are computed for all preferentially-heated species (electron, ion, single-fluid). For all three species, we note that including NEI in the calculation of the cool slope makes essentially no difference .

As in Figure 4, we do not compute the hot slope for the case of ion heating. Looking at the right panel in the middle row of Figure 6, we see that the inclusion of NEI in the case of ion heating has little to no effect on the emission measure. This is confirmed by the left panel of the middle row which shows that the difference between T and T_{eff} is relatively small and only occurs at low densities. Conversely, in the single-fluid and electron-heating cases, T and T_{eff} differ greatly during the heating phase and NEI has two distinct effects on the EM: it leads to an overestimation of the amount of emission in the mid-range hot temperatures ($7.0 \lesssim \log T \lesssim 7.2$) and causes a steeper cutoff in the emission at lower temperatures (before $\log T \approx 7.25$) compared to the case where NEI is not included. Interestingly, in both the electron-heating (first row) and single-fluid (third row) cases, $b_{eff} < b$ though we note that in the electron-heating case (first row), a power-law fit does not adequately describe the hot side of the EM distribution.

To compare the effects of varying α, β, and t_N for each species (i.e. electron, ion, single-fluid), we construct histograms of hot and cool emission measure slopes for each parameter space point. Recall that in the case where the distributions of heating event energies are non-uniform, we have N_R emission measure slopes to properly account
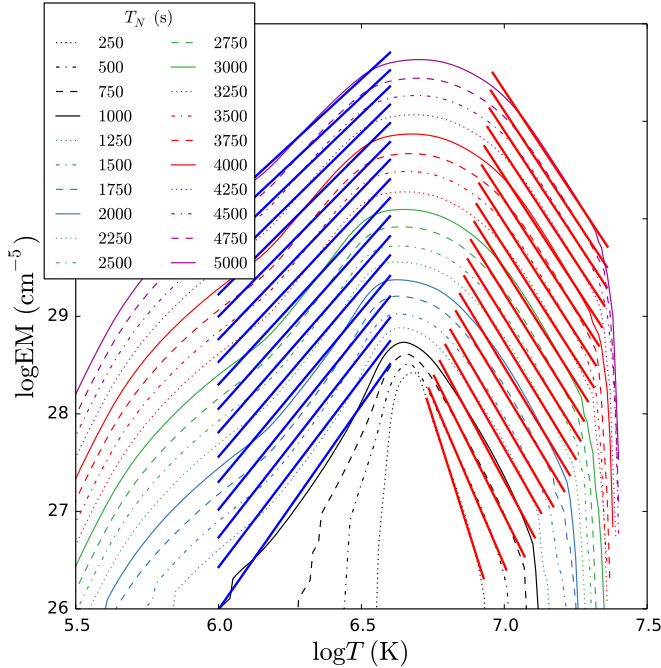
Fig. 5.— Same as Figure 3, but for the single-fluid case in which electron-ion equilibrium is assumed.
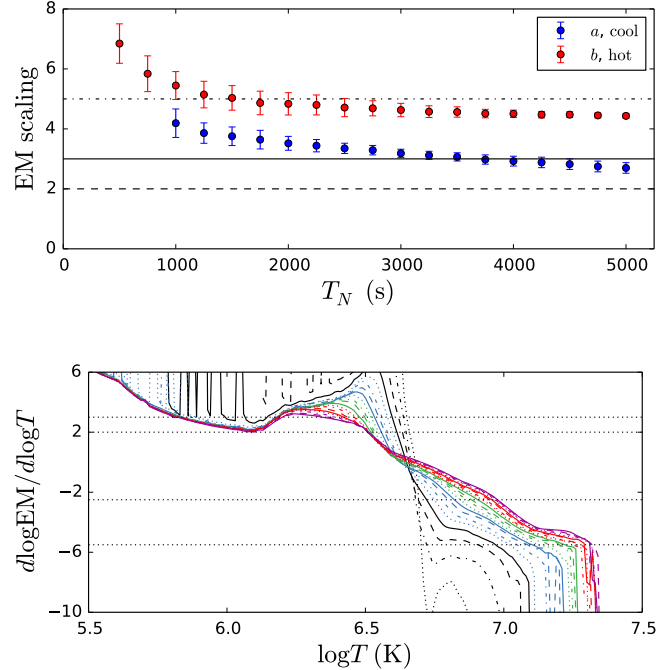
Fig. 6.— Figures for the cases of non-equilibrium ionization.

for the statistical spread in hot emission measure slopes due to power-law distributions.

As seen in Figure 7, these histograms, denoted by type of slope (i.e. hot or cool) and species, are constructed in one of two ways: each distinct histogram (denoted by linestyle and/or color) is either representative of a distinct heating function (e.g. top row of Figure 7) or a distinct value of t_N (e.g. bottom row of Figure 7). In the four panels of Figure 7, we choose to separate the cool emission measure slopes by type of heating function and the hot emission measure slopes by t_N. This means, for example, that the dot-dashed blue $\alpha = -1.5, \beta = 1$ histogram in the upper left panel of Figure 7 encapsulates cool emission measure slopes for $250 \leq T_N \leq 5000$ s while the solid blue $T_N = 2000$ s histogram in the lower left panel includes emission measure slopes for all 10 types of heating functions (as listed in Figure 1 and the legend in the upper left panel of Figure 7). All histograms are normalized such that for each distribution $P(x)$, $\int_{-\infty}^{\infty} dx \, P(x) = 1$. Additionally, the bin widths are calculated using the well-known Freedman-Diaconis formula (Freedman & Diaconis 1981).

Concerning the distributions of cool slopes grouped by type of heating function (bottom row of Figure 7), we note that there are no discernible differences between the cases of electron and ion heating. In both cases, all heating functions except for those where $\beta = 1$ are peaked sharply between 2 and 2.5. In the case where $\beta = 1$ (for all α), the distribution is peaked between 2.5 and 3, with the width of the distribution increasing as α steepens. This larger range of cool emission measure slopes for the case of $\beta = 1$ is consistent with Cargill (2014).

As stated in **??**, we choose not to show the hot emis-

sion measure slopes for the ion heating case as they are not representative of the emission measure distribution hotward of the peak as evidenced by the left and bottom right panels of Figure 4. Instead, we compare the hot emission measure slopes of the electron heating and single-fluid cases, the bottom left and bottom right panels of Figure 7, respectively. In both cases, for $T_N < 3000$ s, we see a strong dependence on t_N while for $T_N \geq 3000$ s, the slopes tend to be sharply peaked around a single value. In the electron heating case, distributions for $T_N < 3000$ s tend to be more narrow than their single-fluid counterparts and centered at lower values (i.e. more shallow hot slopes). Most notably, for $T_N \geq 4000$ s, the electron heating hot emission measure slopes are peaked between 3 and 3.5 while the single-fluid slopes are peaked at ~ 4.5.

4. DISCUSSION

The main points we emphasize from the results presented in Section 3 are,

1. Cool emission measure slopes resulting from electron and ion heating are very similar and are well described by EM $\propto T^a$. As noted in Cargill (2014), using the relation $Q \propto T_N^\beta$ yields $2 \lesssim a \lesssim 5$, consistent with observations.

2. Hot emission from electron heating results in an enhanced hot shoulder while the equivalent ion heating cases show a relatively flat peak and a steep dropoff near 10^7 K. This effect is exacerbated as t_N increases.

3. Hot emission due to both electron and ion heating is poorly described by the scaling EM $\propto T^{-b}$. In the former, this is due to the flat hot shoulder
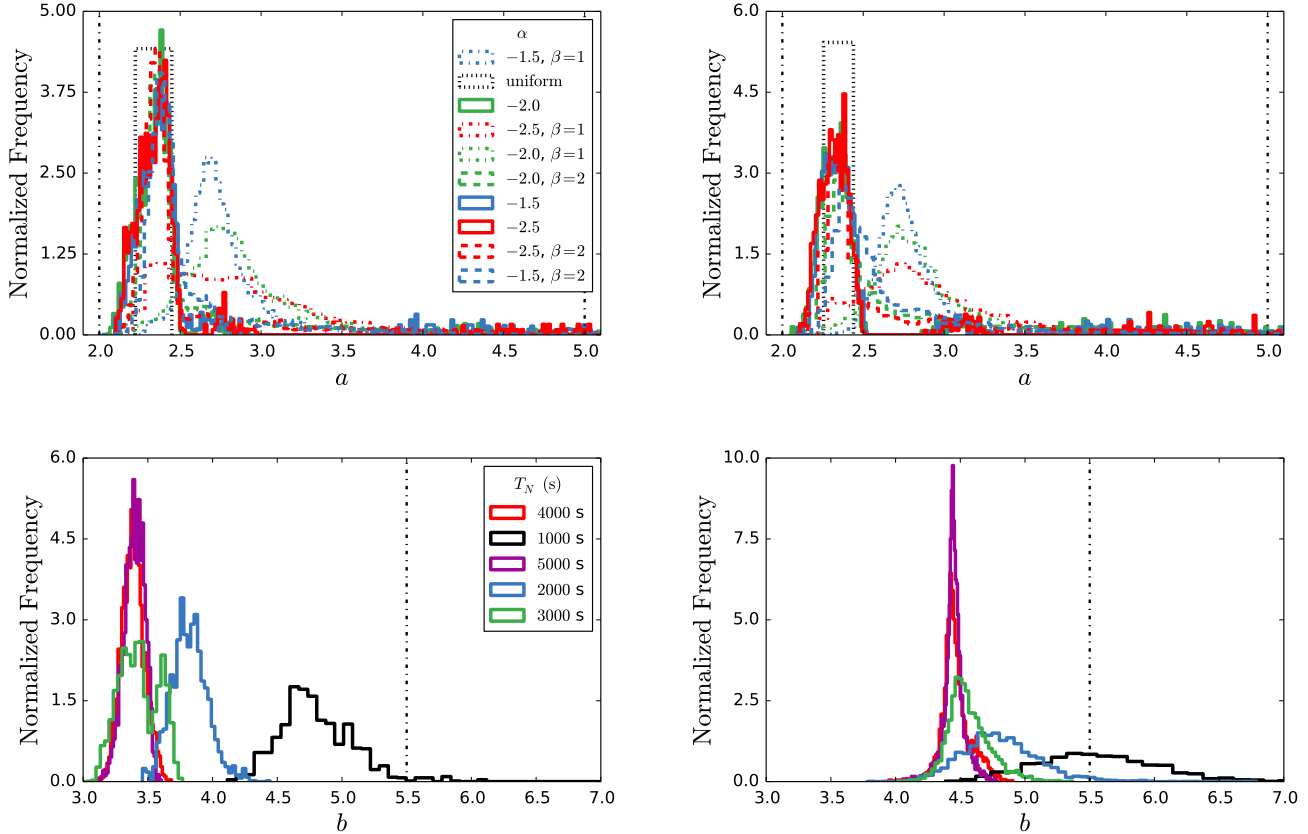
FIG. 7.— Histograms of emission measure slopes from the entire parameter space as described in Figure 1. **Top left:** cool slopes grouped by heating function for the electron heating case; **Top right:** cool slopes grouped by heating function for the ion heating case; **Bottom left:** hot slopes grouped by t_N for the electron heating case; **Bottom right:** hot slopes grouped by t_N value for the single-fluid case. In the cases where the slopes are grouped by t_N, only $T_N = 1000, 2000, 3000, 4000, 5000$ s are shown for aesthetic purposes.

between 10^7 and $10^{7.5}$ K. In the latter case, the relatively flat peak and steep drop off near 10^7 K do not allow for a power-law description of the hot emission.

4. Using a power-law to describe the hot side of the EM distribution, single-fluid models predict less hot-emission than two-fluid models in which only the electrons are heated. In particular, for $T_N \geq 4000$ s, our modified two-fluid EBTEL model predicts $3 \leq b \leq 3.5$ while the original single-fluid EBTEL model predicts $b \sim 4.5$.

5. Including NEI does not impact the cool emission measure slope. In the case of electron heating and the single-fluid case, NEI enhances the mid-range hot EM, but leads to a lower temperature cutoff. The emission measure distribution in the case of ion heating is unaffected.

We first focus on item 1. In the range $6.0 \leq \log T \leq 6.6$, the loop is undergoing both radiative and enthalpy-driven cooling. During this phase, the density is high and the temperature low relative to the heating and conductive cooling phase. Looking at the fourth term on the right-hand side of **??** and **??**, the coupling term between the two species is roughly $\propto \bar{n}^2(\bar{T}_e - \bar{T}_i)/\bar{T}_e^{3/2}$; as density increases, so does the coupling strength. While the loop is also draining in this temperature range, the density has already increased such that $\bar{T}_e \approx \bar{T}_i$ and un-

til the next heating event, there is nothing to drive the two species out of equilibrium. Thus, because the two species are evolving together in this regime, we expect their emission measure distributions to be the same.

In item 2, we see quite the opposite situation. In the heating and conductive cooling phases, the density is relatively low and the electron (or ion) temperature relatively high. Because the heating pulses we have used are relatively short (100 s), the heated species quickly reaches high temperatures and cools significantly by thermal conduction before Coulomb collisions can bring the two species back into equilibrium. Since the emission measure depends on the electron temperature, this means that in the event that only the electrons are heated, the emission "sees" the full range of temperatures produced by heating and conductive cooling.

However, in the case of ion heating, in order for the emission measure to see the full range of temperatures resulting from the heating and conductive cooling by the ions, $\bar{T}_e = \bar{T}_i$ would have to hold for this entire phase. Instead, as the ions are impulsively heated, the electrons remain at a relatively low temperature, coupled only weakly to the ions because the loop has only just begun to fill. As the coronal density increases, the electrons come into equilibrium with the ions, but because thermal conduction is such an efficient cooling mechanism in the corona, the ions have now cooled far below the temperature to which they were initially heated.

The result is a severely truncated hot emission measure distribution as seen in Figure 4. Additionally, this effect is exacerbated at long t_N. For short t_N, the heating is essentially steady, meaning that the loop has little to no time to drain or cool between heating events. This keeps the density at a roughly constant, near-equilibrium value which inhibits rapid heating to high temperatures and keeps the electrons and ions in equilibrium. However, for longer t_N, the loop is allowed to drain significantly between each pulse. Thus, at the start of each heating event, the density is low, allowing the species to very quickly evolve out of equilibrium.

Finally, item 5 addresses the fact that NEI does not affect cool emission or emission due to ion heating, while it acts to enhance mid-range hot temperature emission and creates a lower-temperature cutoff in the single-fluid and electron heating cases as shown in Figure 6. As discussed in Paper I and Section 1, if the heating occurs on a timescale faster than the ionization equilibration timescale, high temperatures will not be detectable because the charge states indicative of such temperatures will not have had time to form. Coolward emission is due to radiative and enthalpy-driven cooling and during this phase, the density is relatively high and the temperature is changing relatively slowly, meaning that ionization equilibrium can be assumed.

For hotward emission in the case of ion heating, we note that the effective heating timescale for the electrons is approximately τ_{ei}, the coupling timescale. For $Q \approx 10^{25}$ erg, the electron temperature increases relatively slowly (compared to the heating timescale of the ions) and only gets above several MK once the density has increased significantly. Thus, ionization equilibrium can be assumed because the electrons undergo no direct impulsive heating. In the cases of electron heating and the single-fluid case, the electrons undergo direct impulsive heating when the density is relatively low. This is what leads to the lower-temperature cutoff in EM_{eff}: at these high temperatures and low densities, the ionization equilibration timescale is significantly longer than the heating timescale and so these very high temperatures are never seen.

However, looking at the left panels in the first and third rows of Figure 6, we see that just after the heating ends at 100 s, $T_{eff} > T$ due to the fact that the thermal conduction timescale is shorter than the ionization equilibration timescale. This lag in the charge state due to the efficiency of thermal conduction leads to the mid-range hot temperature emission enhancement seen in the right panels of the first and third rows of Figure 6.

and wait time, β. We have found that while there is little difference in the cool emission between the cases of electron and ion heating, the emission measure curves of the electron-heated loops have an enhanced hot shoulder due to faster loop filling times and steepened hot mid-range slope due to accelerated cooling by the Coulomb collisions while the ion-heated loops show a truncated emission measure distribution on the hot side. These differences become more prominent as t_N increases. We note that given such a distinction in the EM distribution between the cases of electron and ion heating, the difference could be potentially observationally diagnosable by instruments such as MaGIXS, the Focusing Optics X-ray Solar Imager (FOXSI) (Krucker et al. 2011), or other future missions with adequate spectroscopic resolution in the hard X-rays.

Furthermore, by comparing these results with emission measure distributions obtained from the original single-fluid EBTEL model, we have found that heating only the electrons and using a single power-law fit leads to significantly smaller hot emission measure slopes for equivalent values of t_N. Thus, using a single-fluid model to interpret observed hot emission measure distributions can potentially lead to a misdiagnosis of the heating frequency. Additionally, characterizing the hotward emission with a single power-law fit, as is common practice with cool emission, does not adequately capture all of the features of the hotward emission.

We note that in this study, we have constructed the most ideal emission measure curves by using the expression EM $= n^2(2L)$; that is, we have not taken into account the many complications involved when computing emission measure distributions from observed spectral lines. For example, as we noted in Paper I, impulsive heating leads to NEI and a consequently lower effective temperature, meaning that the emission does not see the hottest temperatures during the conductive cooling phase. By computing test cases for electron heating, ion heating, and the single-fluid case, we have shown that NEI has the effect of steepening the hot emission measure distribution at very high temperatures and enhancing the mid-range hot temperature emission for the electron heating and single-fluid cases, but has no impact on the emission measure distribution in the case of ion heating. We stress that when interpreting observed hot emission in the context of simulation, two-fluid and non-equilibrium ionization effects should be properly taken into account in order to extract meaningful properties of the heating.

5. CONCLUSIONS

In this paper, we have used a modified two-fluid version of the popular EBTEL model to study the effect of preferentially heating the electrons or ions on the hot and cool emission measure slopes over a parameter space that includes the power-law index describing the distribution of event energies, α, waiting time between successive heating events, t_N, and the scaling between the event energy

REFERENCES

Barnes, W. T., Cargill, P. J., & Bradshaw, S. J. 2016, submitted
Bradshaw, S. J. 2009, Astronomy and Astrophysics, 502, 409

Bradshaw, S. J., & Cargill, P. J. 2006, Astronomy and Astrophysics, 458, 987
—. 2013, The Astrophysical Journal, 770, 12

Bradshaw, S. J., & Klimchuk, J. A. 2011, The Astrophysical Journal Supplement Series, 194, 26

Bradshaw, S. J., Klimchuk, J. A., & Reep, J. W. 2012, The Astrophysical Journal, 758, 53

Brosius, J. W., Daw, A. N., & Rabin, D. M. 2014, The Astrophysical Journal, 790, 112

Cargill, P. J. 1994, The Astrophysical Journal, 422, 381

—. 2014, The Astrophysical Journal, 784, 49

Cargill, P. J., Bradshaw, S. J., & Klimchuk, J. A. 2012a, The Astrophysical Journal, 752, 161

—. 2012b, The Astrophysical Journal, 758, 5

Cargill, P. J., & Klimchuk, J. A. 2004, The Astrophysical Journal, 605, 911

Cargill, P. J., Warren, H. P., & Bradshaw, S. J. 2015, Philosophical Transactions of the Royal Society of London Series A, 373, 20140260

Cirtain, J. W., Golub, L., Winebarger, A. R., et al. 2013, Nature, 493, 501

Culhane, J. L., Harra, L. K., James, A. M., et al. 2007, Solar Physics, 243, 19

De Pontieu, B., Title, A. M., Lemen, J. R., et al. 2014, Solar Physics, 289, 2733

Freedman, D., & Diaconis, P. 1981, Zeitschrift für Wahrscheinlichkeitstheorie und Verwandte Gebiete, 57, 453

Golub, L., Deluca, E., Austin, G., et al. 2007, Solar Physics, 243, 63

Hunter, J. D. 2007, Computing in Science & Engineering, 9, 90

Klimchuk, J. A. 2006, Solar Physics, 234, 41

Klimchuk, J. A., Patsourakos, S., & Cargill, P. J. 2008, The Astrophysical Journal, 682, 1351

Kobayashi, K., Cirtain, J., Golub, L., et al. 2011, in Society of Photo-Optical Instrumentation Engineers (SPIE) Conference Series, Vol. 8147, 81471M

Kosugi, T., Matsuzaki, K., Sakao, T., et al. 2007, Solar Physics, 243, 3

Krucker, S., Christe, S., Glesener, L., et al. 2011, in Society of Photo-Optical Instrumentation Engineers (SPIE) Conference Series, Vol. 8147, 814705

Parker, E. N. 1988, The Astrophysical Journal, 330, 474

Pérez, F., & Granger, B. E. 2007, Computing in Science & Engineering, 9, 21

Reale, F., & Orlando, S. 2008, The Astrophysical Journal, 684, 715

Reale, F., Testa, P., Klimchuk, J. A., & Parenti, S. 2009, The Astrophysical Journal, 698, 756

Schmelz, J. T., Saar, S. H., DeLuca, E. E., et al. 2009, The Astrophysical Journal Letters, 693, L131

Testa, P., De Pontieu, B., Martínez-Sykora, J., et al. 2013, The Astrophysical Journal Letters, 770, L1

Testa, P., De Pontieu, B., Allred, J., et al. 2014, Science, 346, 1255724

van der Walt, S., Colbert, S. C., & Varoquaux, G. 2011, Computing in Science & Engineering, 13, 22

Warren, H. P., Brooks, D. H., & Winebarger, A. R. 2011, The Astrophysical Journal, 734, 90

Warren, H. P., Winebarger, A. R., & Brooks, D. H. 2012, The Astrophysical Journal, 759, 141

Winebarger, A. R. 2014, AGU Fall Meeting Abstracts, 52, 03

Winebarger, A. R., Warren, H. P., Schmelz, J. T., et al. 2012, The Astrophysical Journal Letters, 746, L17